International Journal of Mechanical, Industrial and Aerospace Sciences
ISSN: 2517-9950
Vol:11, No:12, 2017

Study of the S-Bend Intake Hammershock Based on Improved Delayed Detached Eddy Simulation

Qun-Feng Zhang, Pan-Pan Yan, Jun Li, Jun-Qing Lei

***Abstract*—**Numerical investigation of hammershock propagation in the S-bend intake caused by engine surge has been conducted by using Improved Delayed Detach-Eddy Simulation (IDDES). The effects of surge signatures on hammershock characteristics are obtained. It was shown that once the hammershock is produced, it moves upward to the intake entrance quickly with constant speed, however, the strength of hammershock keeps increasing. Meanwhile, being influenced by the centrifugal force, the hammershock strength on the larger radius side is much larger. Hammershock propagation speed and strength are sensitive to the ramp upgradient of surge signature. A larger ramp up gradient results in higher propagation speed and greater strength. Nevertheless, ramp down profile of surge signature have no obvious effect on the propagation speed and strength of hammershock. Increasing the maximum value of surge signature leads to enhance in the intensity of hammershock, they approximately match quadratic function distribution law.

***Keywords*—**Hammershock, IDDES, S-bend, surge signature.

I. Introduction

HAMMERSHOCK is a strong compression wave formed at the engine face immediately following stall. When hammershock is generated, it propagates upward along the intake rapidly, and the maximum pressure of hammershock can reach as large as two times of the inflow total pressure [1]-[4]. As a result the intake wall will suffer heavy pressure load and it has a great influence on the design of intake structure. Nowadays, due to the aerodynamic configuration, more and more S-bend intakes are used in the aircraft. Because of the influence of the bending section, the hammershock load will be much greater. Therefore, it is necessary to study the process of the generation and development of the hammershock in the S-bend intake.

Since the hammershock is caused by engine stall, the surge signature is a key factor. Some former research works have been carried out about the surge signatures. Goble [5] invested surge of YF119 engine with 'guillotine' method and he claimed that the ramp up and ramp down of surge signatures were sinusoidal in nature and stall events may last for over 30 ms. Webb and Heron [6] hold a different view and considered the signature was a sharp initial rise in positive over-pressure to a peak within 1ms. Causon [7] believed that the surge took the form of a linear rise to a peak Over Pressure Ratio (OPR) within 2.5 ms followed by a linear recession back to a normal OPR. Ytterstorm [8] considered the pressure rise to a peak was approximately liner and then dropped back to a normal pressure in linear fashion too. As can be seen, there is no universally accepted surge signature, so several different surge signatures have been considered in the present work.

Qun-Feng Zhang is with the Department of Mechanics, School of Civil Engineering, Beijing Jiaotong University, Beijing, 100044, China, (e-mail: zhangqunfeng@263.net).
Pan-Pan Yan is with the Department of Mechanics, School of Civil Engineering Beijing Jiaotong University, Beijing, 100044, China.
Jun Li is with Shenyang Aircraft Design and Research Institute, Aviation Industry of China, Shenyang, 110035, Liaoning, China.
Jun-Qing Lei is with the School of Civil Engineering, Beijing Jiaotong University, Beijing, 100044, China.

II. Methodology

A. Governing Equations

For store separation problems, the modified form of the Navier-Stokes equations which account for the relative motion of the grid with respect to the fluid are as [9]:

$$\frac{\partial}{\partial t}\int_{\Omega} \boldsymbol{W} d\Omega + \oint_{\partial\Omega} \left(\boldsymbol{F_c} - \boldsymbol{F_v}\right) dS = 0 \tag{1}$$

where $\boldsymbol{W}$ denotes conservative variables, $\boldsymbol{F_c}$ represents the vector of the convective fluxes, $\boldsymbol{F_v}$ stands for the vector of viscous fluxes, $\boldsymbol{Q}$ is the source term, Ω denotes control volume, and dS represents the surface element. The conservative variables:

$$\boldsymbol{W} = \left[\rho \quad \rho u \quad \rho v \quad \rho w \quad \rho E\right]^T \tag{2}$$

where $\rho, u, v, w,$ E denote the density, the Cartesian velocity components and the total energy per unite mass, respectively.

$$\boldsymbol{F_c} = \begin{bmatrix} \rho V \\ \rho u V + n_x p \\ \rho v V + n_y p \\ \rho w V + n_z p \\ \rho H V \end{bmatrix} \tag{3}$$

where V is contravariant velocity.

$$V \equiv \vec{v} \cdot \vec{n} = n_x u + n_y v + n_z w \tag{4}$$

$$\boldsymbol{F_v} = \begin{bmatrix} 0 \\ n_x \tau_{xx} + n_y \tau_{xy} + n_z \tau_{xz} \\ n_x \tau_{yx} + n_y \tau_{yy} + n_z \tau_{yz} \\ n_x \tau_{zx} + n_y \tau_{zy} + n_z \tau_{zz} \\ n_x \Theta x + n_y \Theta y + n_z \Theta z \end{bmatrix} \tag{5}$$

$$\boldsymbol{Q}=\begin{bmatrix} 0 \\ \rho f_{e,x} \\ \rho f_{e,y} \\ \rho f_{e,z} \\ \rho \boldsymbol{f_e}\cdot\boldsymbol{v}+\dot{q}_h \end{bmatrix} \tag{6}$$

n_x, n_y, n_z denote the components of the outward facing unit normal vector of the surface $\partial\Omega$, where $\tau_{ij}(i=x,y,z;j=x,y,z)$ represents viscous stress, $\boldsymbol{f_e}$ denotes the body force, $f_{e,x}$, $f_{e,y}$ $f_{e,x}$、$f_{e,y}$、$f_{e,z}$ are the three components of $\boldsymbol{f_e}$, $\dot{q}_h$ is heat fluxes density.

The governing equations are discretized using a cell-centered finite-volume method and solved by the dual time-step approach with the inner iteration proceeded by a LU-SGS method. The convective terms are discretized using second-order upwind scheme with the Modified Venkatakrishnan gradient reconstruction limiter to prevent spurious oscillations around shaock wave, while the viscous flux terms are discretized by adopting a central-difference method.

B. IDDES Method

To include the effect of turbulence, the IDDES [10] was adopted in the simulations. IDDES method is based on the SST k-ω turbulence model [11] with the turbulence length scale in the destruction term D_k of k equation replaced by the IDDES length scale [12].

The k-ω turbulence model reads:

$$\frac{\partial \rho k}{\partial t}+\nabla\cdot\left(\rho\vec{U}k\right)=\nabla\cdot\left[\left(\mu+\sigma_k\mu_t\right)\nabla k\right]+P_k-D_k \tag{7}$$

$$\frac{\partial \rho\omega}{\partial t}+\nabla\cdot\left(\rho\vec{U}\omega\right)=\nabla\cdot\left[\left(\mu+\sigma_\omega\mu_t\right)\nabla\omega\right]+ 2\left(1-F_1\right)\rho\sigma_{\omega 2}\frac{\nabla k\cdot\nabla\omega}{\omega}+\alpha\frac{\rho}{\mu_t}P_k-\beta\rho\omega^2 \tag{8}$$

where k is turbulence kinetic energy, t is time, μ is the molecular viscosity coefficient, μ_t is turbulent viscosity coefficient, P_k is production term, D_k is diffusion term, ω is turbulent dissipation ratio and α, β, σ_k, σ_ω, and $\sigma_{\omega 2}$ are constant. The IDDES length scale is given by:

$$D_k=\frac{\rho\sqrt{k^3}}{l_{IDDES}} \tag{9}$$

$$l_{IDDES}=\tilde{f}_d\cdot\left(1+f_e\right)\cdot l_{RANS}+\left(1-\tilde{f}_d\right)\cdot l_{LES} \tag{10}$$

$$l_{LES}=C_{DES}\Delta \tag{11}$$

$$l_{RANS}=\frac{\sqrt{k}}{C_\mu\omega} \tag{12}$$

$$C_{DES}=(1-F_1)C_{DES}^{k-\varepsilon}+F_1C_{DES}^{k-\omega} \tag{13}$$

$$\Delta=\min\left\{\max\left[c_w d_w, c_w h_{max}, h_{wn}\right], h_{max}\right\} \tag{14}$$

where h_{wn} is the grid step in the wall-normal direction, d_w is the distance to the wall, h_{max} is maximum value of h_{wn} and c_w is an empirical constant.

Compared to the original DES97 [13] and DDES [14], IDDES inherits their advantages and overcome several problems such as log-layer mismatch, grid-induced separation and modelled stress depletion.

C. Validation

To evaluate the accuracy of the numerical method chosen in this paper, an S-duct experiment model was simulated and compared with the experimental results given in [15]. The geometric parameters and aerodynamic conditions are consistent with the experimental ones. Fig. 1 shows the geometry of the intake.

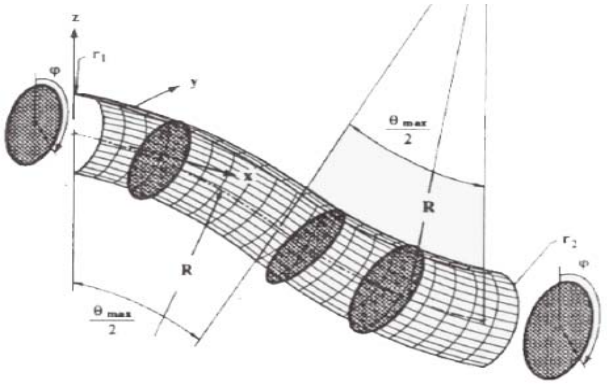

Fig. 1 Sketch of S-duct

The wind tunnel test was conducted with an intake centerline Mach number of 0.6. The Reynolds number based on the intake diameter and centerline velocity is 2.6×10^6. There are two curved segments in the intake. When the fluid flows in the pipe, the internal rotation is generated under the action of the transverse pressure gradient and leads to secondary flow [16]-[18], as shown in Fig. 2.

Fig. 3 shows the axial distribution of surface static pressures for three circumferential positions ($\phi=10^\circ$, $\phi=90^\circ$, $\phi=170^\circ$), ϕ is defined in Fig. 1. The data is obtained by taking time average of the unsteady results. The solid curves represent the simulation results while the dots are experimental results. The results of numerical simulation and experiment fit very well which demonstrates the reliability and the accuracy of the CFD method.

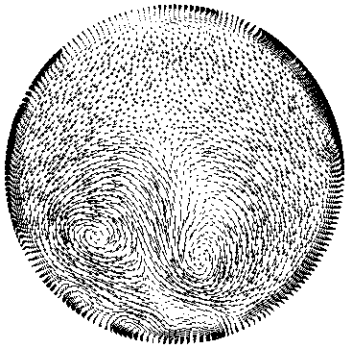

Fig. 2 Computed secondary flow in outlet cross section

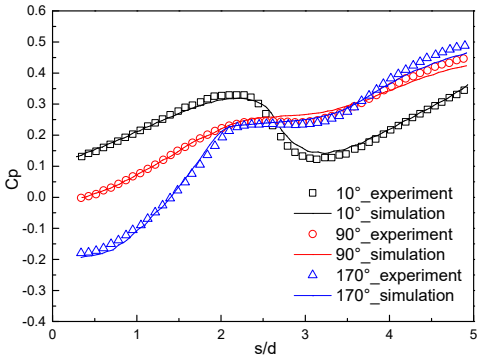

Fig. 3 Axial distribution of surface static pressures at three circumferential positions

III. Computational Case

A. Simulation Model and Meshing

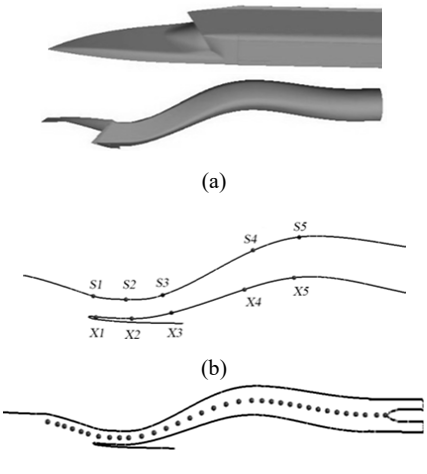

Fig. 4 Geometry of S-bend intake and distribution of pressure monitoring points

Fig. 4 (a) shows the geometry of the S-bend intake with front fuselage, the size of the model is 10 m × 2 m × 2 m. Ten monitoring points were placed on the upper and lower wall of the intake as shown in Fig. 4 (b). In addition, along the intake centerline another 338 monitoring points were set up to capture the propagation of hammershock inside of the intake, every one of ten points were illustrated in Fig. 4 (c).

Fig. 5 shows the mesh distribution of a section (named section_A) which crosses the bump of intake. Polyhedral meshes were generated with a mesh size about 6 mm within the intake. The total number of grid cells is 6 million. In order to assure y+~1, thickness of the first layer mesh next to the wall is 2×10^{-3} mm.

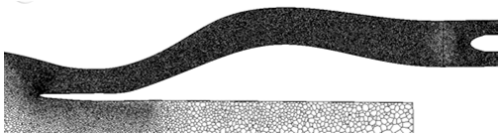

Fig. 5 Grid distribution of section_A

B. Simulation Cases

Ten different surge signatures were considered as shown in Fig. 6. Type 1-Type 3 have a sharp initial rise in positive OPR to the peak value 1.8 and then ramp down in different ways, the whole process lasts for 20 ms. Type 4-Type 6 takes the form of a linear rise to the peak OPR, but with different ramp up gradient and the duration of time is still 20ms. Type 7-Type 10 is similar to Type 3 but has different OPR peak value equal 1.4, 1.6, 2.0, and 2.2.

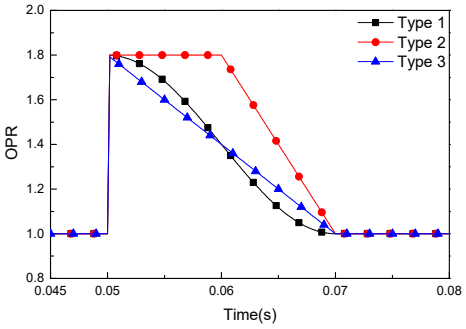

(a)

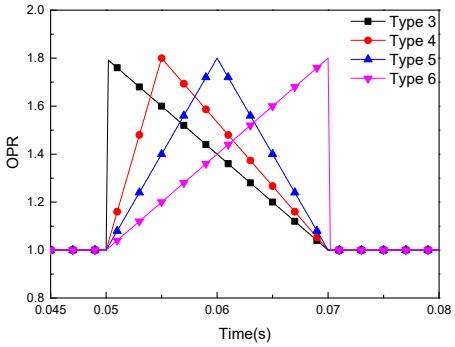

(b)

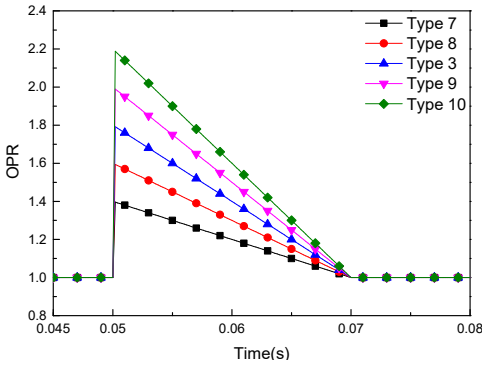

(c)

Fig. 6 Different surge signatures

Both subsonic and supersonic conditions were simulated. For subsonic condition, the inflow Mach number is 0.9, flight altitude is 0 km, and angle of attack is 0°. For supersonic condition, the inflow Mach number is 1.5, flight altitude is 7 km, and angle of attack is 0°. A total 15 cases were simulated for different inflow Mach numbers and surge signatures. Detailed conditions are shown in Table I.

TABLE I
SIMULATION CASES

Case	Ma	Mass flow	OPR form	OPR value
Case 1	0.9	77.7 Kg/s	Type 1	1.8
Case 2	0.9	77.7 Kg/s	Type 2	1.8
Case 3	0.9	77.7 Kg/s	Type 3	1.8
Case 4	0.9	77.7 Kg/s	Type 4	1.8
Case 5	0.9	77.7 Kg/s	Type 5	1.8
Case 6	0.9	77.7 Kg/s	Type 6	1.8
Case 7	0.9	77.7 Kg/s	Type 7	1.4
Case 8	0.9	77.7 Kg/s	Type 8	1.6
Case 9	0.9	77.7 Kg/s	Type 9	2.0
Case 10	0.9	77.7 Kg/s	Type 10	2.2
Case 11	0.9	76 Kg/s	Type 11	1.4
Case 12	0.9	76 Kg/s	Type 12	1.6
Case 13	0.9	76 Kg/s	Type 13	1.8
Case 14	0.9	76 Kg/s	Type 14	2.0
Case 15	0.9	76 Kg/s	Type 15	2.2

IV. Results and Discussion

A. S-Bend Intake Flow Field without Hammershock

During the simulation, the flow rate boundary condition on exit section was set to satisfy different inflow Maher numbers, and the average pressure on the exit section of intake was obtained. For Ma=0.9 cases, the average pressure is P=124757 Pa and for Ma=1.5 cases, the average pressure is P=109886 Pa. This value is used as the reference pressure when calculating the OPR for surge signature.

Fig. 7 shows the Mach number counters of the section_A under normal operating state for both subsonic and supersonic conditions. When the flow Maher number is 0.9, the whole flow field is high subsonic flow except the area near the intake lip. When the inflow Mach number increase to 1.5, an oblique shock wave is formed at the leading edge of the intake, and then a normal shock wave is formed at the intake port, after which the flow become subsonic. There is no obvious pair vortexes observed.

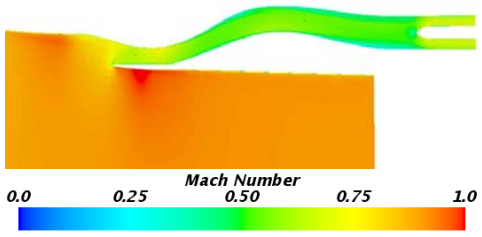

(a)

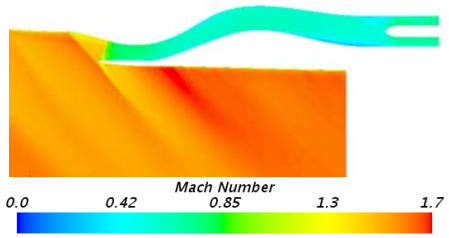

(b)

Fig. 7 Ma counters of section_A for normal operating state

B. S-Bend Intake Flow Field with Hammershock

After the flow field has been established, the flow rate boundary condition on the exit section of intake was changed to pressure outlet boundary condition and the calculation was continued until the flow rate on the the exit section is relative stable. A user defined function was used to set the 10 surge signatures which are mentioned in Fig. 6.

Once the pressure on the exit section of intake changes, the hammershock shows up immediately. Fig. 8 is the Mach number counters of the section_A at different time for case 3. After the hammer shock was formed (t=0.05s), it propagates upward along the intake rapidly. The flow velocity after the hammershock is greatly reduced and there is obvious counter flow near the wall. After t=0.046s the hammershock pass through the entrance of the intake. Fig. 9 shows the pressure distributions at different time. The pressure of hammershock is extremely high and generates great pressure load which will bring serious threat to the structural safety of the intake. Due to the effect of the intake section area, the flow speed near the intake entrance is relative high. As a result, the strength of the hammershock increases when it propagates upward. Meanwhile, influenced by the centrifugal force field, the pressure distributions on the front surface of hammershock are uneven.

Fig. 10 shows the pressure on the intake wall versus time, and the pressure was nondimensionalized using:

$$P_n = \frac{P}{P_{locale}} \quad (15)$$

where P is instantaneous pressure, $\overline{P_{locale}}$ represents the local average pressure without hammershock. So P_n represents the increased multiple of pressure influenced by hammershock.

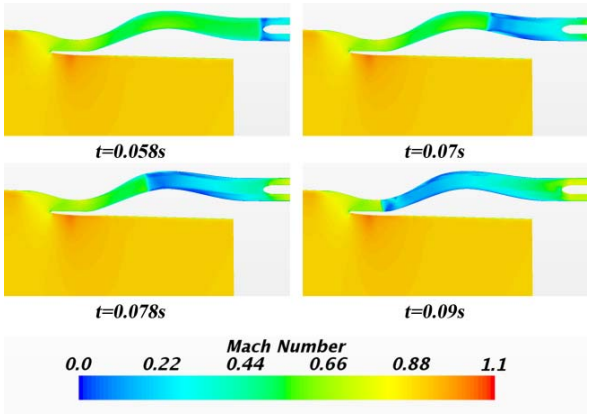

Fig. 8 Ma counters of section_A for different time

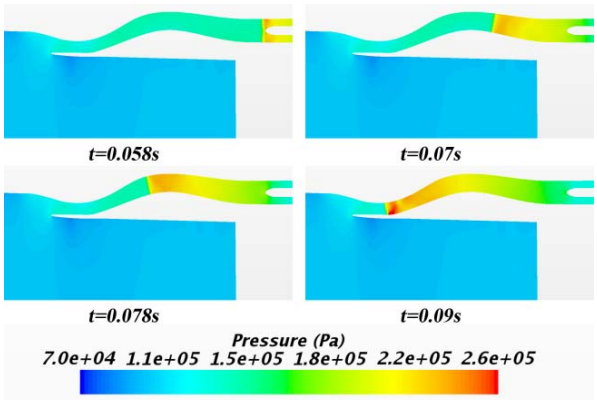

Fig. 9 Pressure counters of section_A at different time

Pressure amplitude varies between different monitoring points, the closer to the entrance, the higher the pressure rise. The maximum pressure of point S1 and X1, which are located near the entrance, is much higher than others. Meanwhile, the maximum pressure of point S4, S5 is higher than the one of X4, X5 and pressure of X2, X3 is higher than S2, S3. Fig. 4 (b) shows that, point S4, S5, X2, X3 are set on the larger radius side, so it reveals that affected by the centrifugal force field, the aerodynamic load on side wall with the larger radius is greater.

Fig. 11 shows the pressure data from the 338 points along centerline of the intake, which give the pressure changes versus time in the S-bend intake. A curvilinear coordinate system is built along the centerline of the intake, and the entrance is set as the original point. Under the curve coordinate system the length of the centerline is L, and set the distance from monitoring points to entrance as x. In Fig. 11, the abscissa represents x/L, where $x/L=0$ represents the entrance of the intake and $x/L=1$ is the exit section of the intake, the ordinate represents time and the color bar represents the value of P_n. Fig. 11 shows an obvious pressure wave transmits from the exit section to the entrance. This pressure wave is just the hammershock. The slope of the dividing line between high pressure zone and low pressure zone is the propagation speed of the hammershock, which equals approximately to the combination of the local sound speed and the local flow speed. The dividing line is a straight line which means the hammershock propagates in constant speed which is about 180 m/s. The pressure difference between wave front and wave rear keeps increasing when the hammershock transmits upward, and reaching its maximum P_n =2 at $x/L=0$. When the hammershock reaches the location $x/L<0$, it propagates out of the intake with an obvious attenuation in strength.

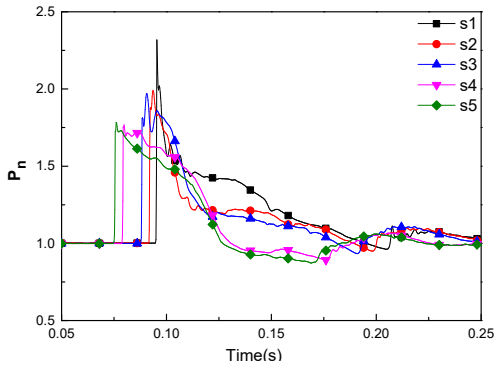

(a)

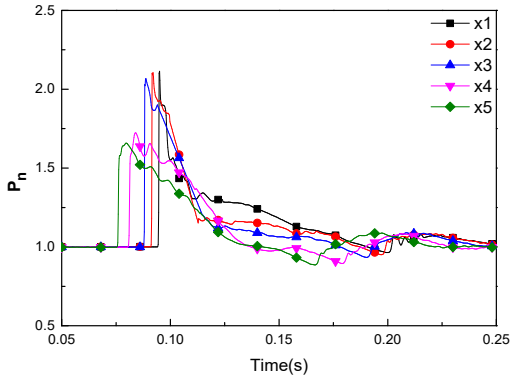

(b)

Fig. 10 P_n of monitoring points versus time on the surface

C. Influence of Surge Signature to Hammershock

1. Different pressure ramp down profile

Assume that when the engine stall happens the ramp up profiles of the surge signatures keep the same and the ramp down profiles are different, as shown in Fig. 6 (a) type 1 to type 3. The ramp down profile of type 1 is cosinusoid, type 2 keeps the maximum pressure for a while and then ramps down linearly, and type 3 ramps down linearly immediately. The variation in time is 20ms, and the maximum OPR is 1.8. These

surge signatures correspond to simulation case 1 to case 3.

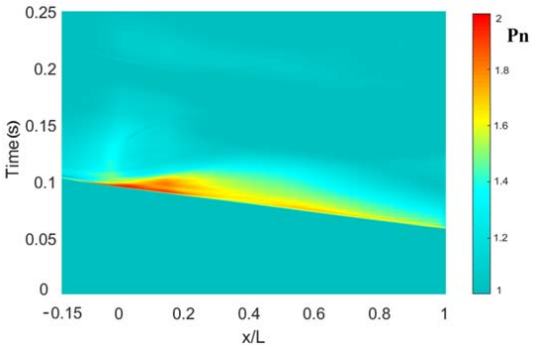

Fig. 11 Pressure of centerline versus time in the S-bend intake

Fig. 12 shows the pressure change of monitoring points S1 to S5 versus time for case1 to case 3. Monitoring point S1has the maximum amplitude of pressure increases and the corresponding P_n are 2.37, 2.41, and 2.36. In case 2, the pressure amplification is higher than the other two. The reason is that type 2 surge signature keeps its maximum pressure for a little longer, and more energy was inputted into the system. However, the difference between three cases is tiny, different pressure ramp down profiles have little effect on hammershock strength.

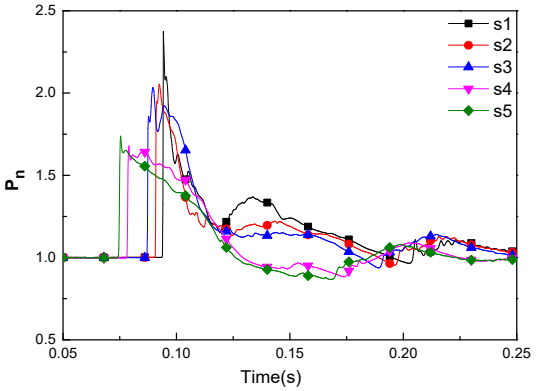

(a) Case 1

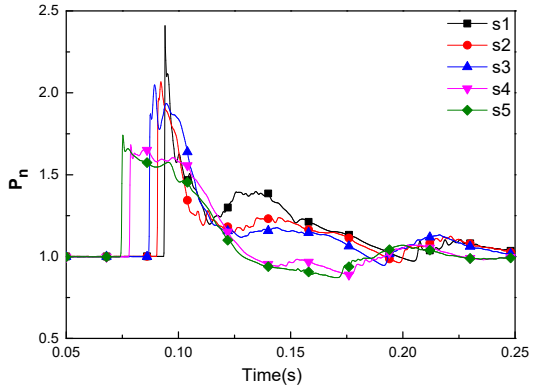

(b) Case 2

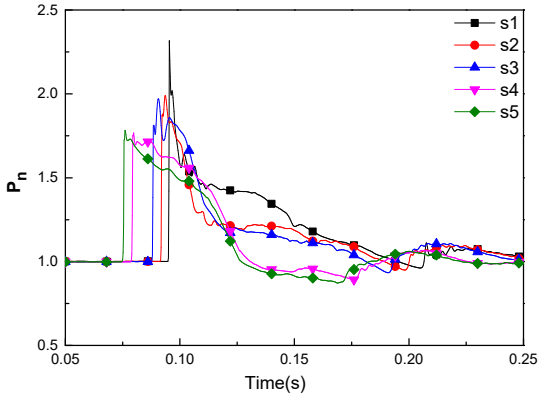

(c) Case 3

Fig. 12 P_n of monitoring points versus time on the surface for different cases

2. Different Pressure Ramp up Profiles

Assume that when the engine stall happens the ramp up profiles of the surge signature are different, meanwhile, the variation time and the maximum OPR is kept as 20 ms and 1.8, respectively, as shown in Fig. 6 (b), type 3 to type 6. Type 3 has the maximum pressure ramp up gradient while type 6 has the minimum pressure ramp up gradient. The average pressure of the exit section of intake keeps the same for different surge signatures.

Fig. 13 shows the pressure changes of monitoring points S1 to S5 versus time for case 1 to case 3. The maximum amplitude of pressure increase is still in monitoring point S1, whereas the values of P_n vary obviously. The value of P_n corresponding to case 3 to case 6 equals 2.36, 2.15, 2.04 and 1.85, respectively. As the ramp up gradient decreases, the strength of the hammershock decreases gradually. The time of reaching the maximum pressure for different cases is not the same which means the propagation speeds of the hammershock are different.

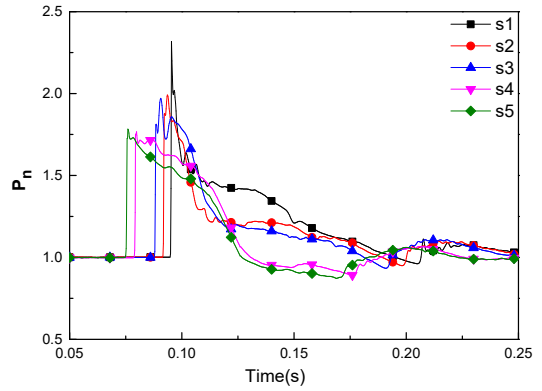

(a) Case 3

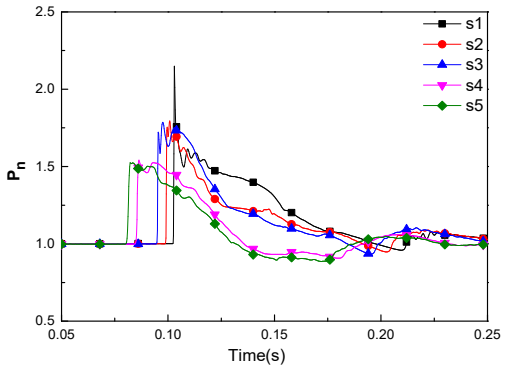

(b) Case 4

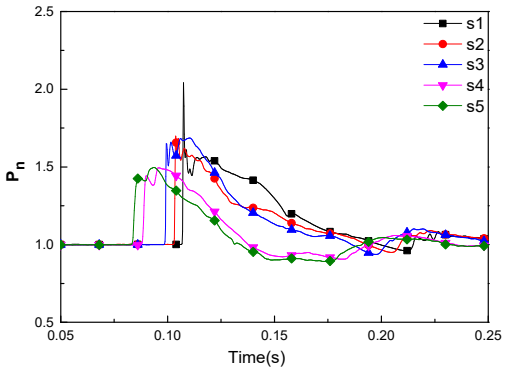

(c) Case 5

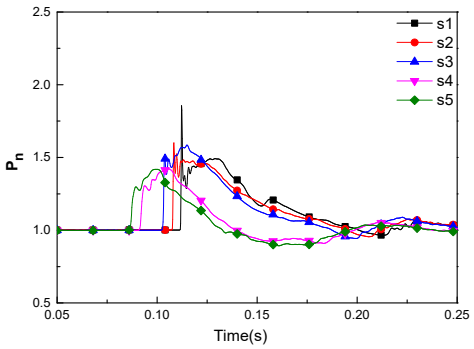

(d) Case 6

Fig. 13 P_n of monitoring points versus time for case3 to case 6

Fig. 14 shows the speed of sound of the section_A for different cases, the local sound speed near the hammershock front decreases with the reduction of ramp up gradient. Fig. 15 shows the pressure change versus time in the S-bend intake. From measuring the slope of the dividing lines between high pressure zone and low pressure zone and different hammershock propagation speeds were obtained which are 180 m/s, 159 m/s, 149 m/s and 142 m/s for case 3 to case 6, respectively. The larger of ramp up gradient, the faster the hammershock propagates.

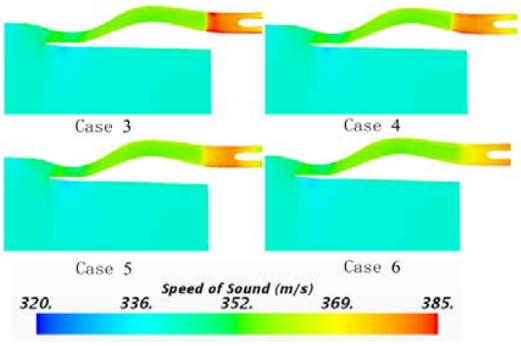

Fig. 14 Speed of sound for different cases

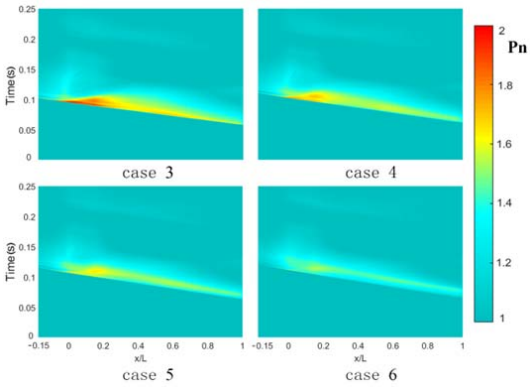

Fig. 15 Pressure of centerline vs time in the S-bend intake for different cases

3. Different Maximum Value of OPR

Assume that when the engine stall happens, the ramp up and ramp down profiles of the surge signature keep the same, while the maximum value of OPR varies as 1.4, 1.6, 1.8, 2.0 and 2.2 for type 7, type 8, type 3, type 9 and type 10, respectively. Both subsonic inflow and supersonic inflow conditions were simulated. Fig. 16 shows the pressure changes versus time of monitoring points S1 to S5. Under both subsonic and supersonic inflow conditions, the maximum value of P_n increases with the increase of maximum OPR. The detailed values are listed in Table II.

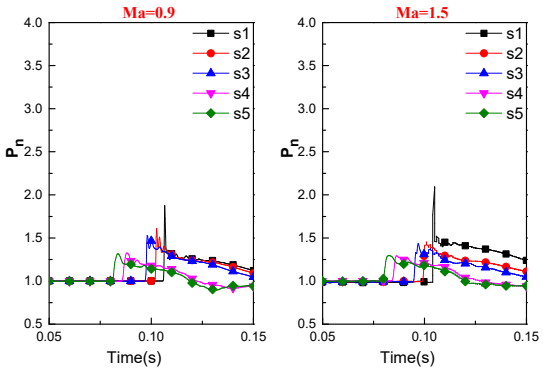

(a) OPR=1.4

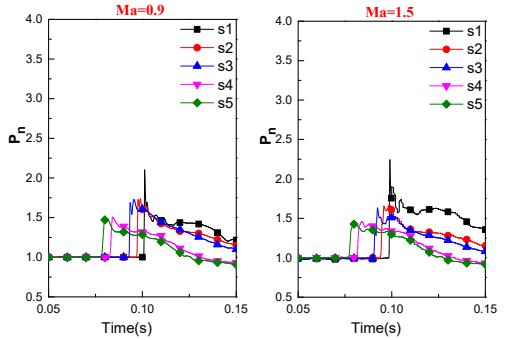

(b) OPR=1.6

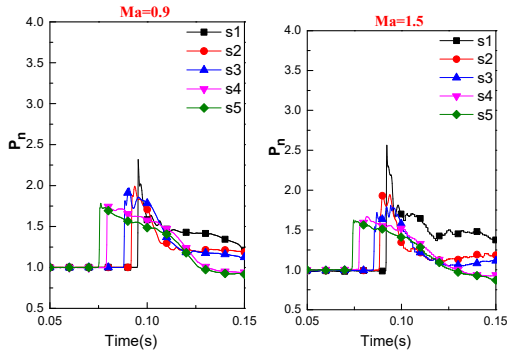

(c) OPR=1.8

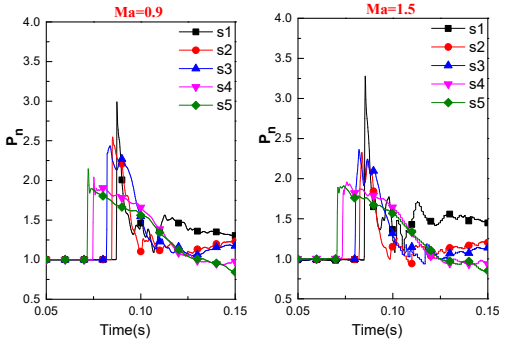

(d) OPR=2.0

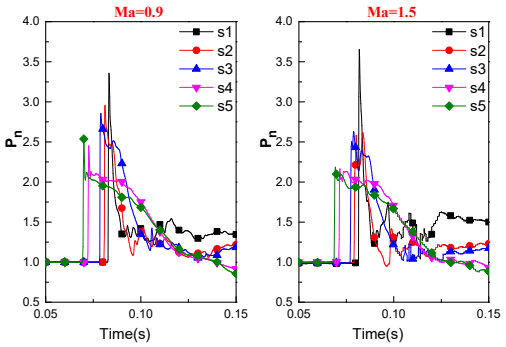

(e) OPR=2.2

Fig. 16 P_n of monitoring points vs time for different cases

TABLE II
P_n FOR DIFFERENT OPR

OPR	1.4	1.6	1.8	2.0	2.2
Ma=0.9	1.8	2.1	2.3	3	3.35
Ma=1.5	2.09	2.24	2.56	3.27	3.66

Fig. 17 shows the varying pattern of maximum P_n with OPR, the dots represent the simulation results while the solid curves are fitting curves. The maximum value of P_n and OPR are approximately in accordance with the law of quadratic function. Under supersonic inflow the varying pattern is similar to subsonic inflow, however, the maximum value of P_n is larger than the subsonic condition about 0.3.

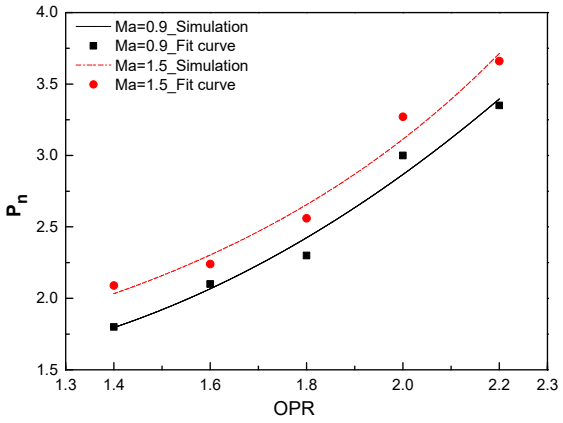

Fig. 17 Varying pattern of maximum P_n with OPR

Fig. 18 shows the pressure change versus time in the S-bend intake for different maximum OPR conditions. For both subsonic and supersonic conditions with the increase of the maximum OPR, the pressure difference before and after hammershock increases which means the strength of hammershock being enhanced. Meanwhile the slope of the dividing line gets larger which means the propagation speed of hammershock increases with the increase of the maximum OPR too. The detailed values are listed in Table III.

When the maximum OPR=2.0 or OPR=2.2, the hammershock presents a distinct oscillation process near the intake. It means the interactions between inflow and hammershock become stronger with the inflow Mach number increase from 0.9 to 1.5.

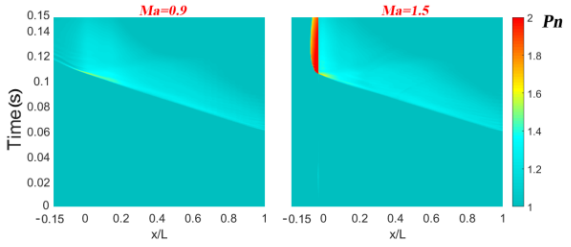

(a) OPR=1.4

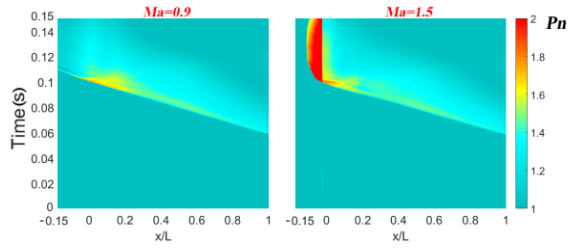

(b) OPR=1.6

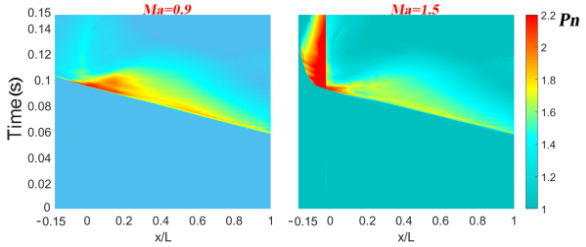

(c) OPR=1.8

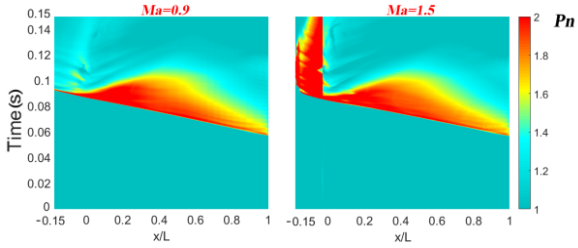

(d) OPR=2.0

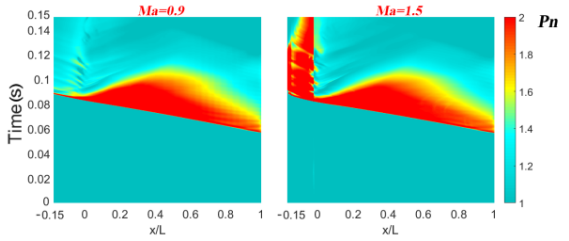

(e) OPR=2.2

Fig.18 Pressure of center line vs time in the S-bend intake for different maximum OPR

TABLE III
HAMMERSHOCK VELOCITY FOR DIFFERENT OPR

OPR	1.4	1.6	1.8	2.0	2.2
Ma=0.9	144 m/s	160 m/s	180 m/s	220 m/s	253 m/s
Ma=1.5	149 m/s	170 m/s	190 m/s	235 m/s	256 m/s

V. CONCLUSIONS

The hammershock properties in the S-bend intake were studied by using IDDES method, the effects of different surge signatures were obtained. The following conclusions can be drawn from this study.

1) When hammer shock is generated, it propagates upward along the intake rapidly with approximate constant speed and the strength of hammer shock increases. Meanwhile aerodynamic load of S-bend intake inner wall is uneven under the influence of the centrifugal force field. The aerodynamic load on side wall with the larger radius is greater.
2) Ramp down profiles of surge signatures have no obvious effects on the hammer shock propagation speed and strength.
3) Increasing the ramp up gradient of surge signature leads to enhance in hammer shock propagation speed and strength. In our case the propagation speeds increase from 142 m/s to 180 m/s and P_n rise from 1.85 to 2.36.
4) The intensity of hammer shock increases with the growth of maximum value of OPR. They approximate match quadratic function distribution law. The hammer shock intensity of supersonic inflow is greater than the one of subsonic inflow.

REFERENCES

[1] R. D. Menzies, K. J. Babcock, G. N. Barakos, "Surge Wave Propagation Modelling Using Computational Fluid Dynamics," in *Proc. 21st Applied Aerodynamics Conference*, Florida, 2003, pp. 1–12.
[2] A. P. Kurkov, R. H. Soeder, J. E. Moss, "Investigation of the stall hammershock at the engine intake," *Journal of Aircraft*, vol. 12, no. 4, pp. 198–204, Apr. 1975.
[3] A. R. Porro, "On Hammershock Propagation in a Supersonic Flow Field," in *Proc. 23rd Congress of the International Council of the Aeronautical Sciences*, Toronto, 2002, 11-25.
[4] Y. Zhu, T. R. Shen, "Evaluation Approach of Hammershock Loading for Aircraft Inlet," *Aeroengine*, vol. 41, no. 3, pp. 6–11, Mar. 2015.
[5] B. Goble, S. King, "Inlet hammershock analysis using a 3-D unsteady Euler/Navier-Stokes code," in *Proc. 32nd Joint Propulsion Conference and Exhibit*, Florida,1996, pp. 21–45.
[6] D. R. Webb, H. K. Heron, "The effect of engine surge on intake-structure loads," *The royal aircraft establishment*, London, 1-9, 1979.
[7] D. Causon, D. Ingram, "Numerical simulation of engine surge in a twin side-by-side intake system," *The Aeronautical Journal*, vol. 25, no. 3, pp. 365–370, Mar. 1997.
[8] A. Ytterstorm, E. Axelson, "Hammershock Calculations in the Air Intake of JAS 39 GFUPEN, using Dual Timestepping," in *Proc. 17th Applied Aerodynamics Conference*, Florida, 1999, pp. 232–251.
[9] J. Blazek, "Computational fluid dynamics principles and applications," 2nd ed. Elsevier, London, 2005, pp. 16–18.
[10] M. L. Shur, R. R. Spalart, M. Strelets, "A hybrid RANS-LES approach with delayed-DES and wall-modelled LES capabilities," *International Journal of Heat and Fluid Flow*, vol. 29, pp. 1638–1649, July 2008.
[11] F. R. Menter, "Two-equation eddy-viscosity turbulence modeling for engineering applications," *AIAA Journal*, vol. 32, pp. 1598-1605, May 1994.
[12] M. Strelets, "Detached eddy simulation of massively separated flows," in *Proc. 39th Aerospace Sciences Meeting and Exhibit*, Reno, 2001, pp. 132–155.
[13] P. R. Spalart, W. H. Jou, M. Strelets, "Comments on the feasibility of LES for wings, and on a hybrid RANS/LES approach," *Advances in DNS/LES*, vol. 15, pp. 4-8, Aug. 1997.
[14] P. R. Spalart, S. Deck, M. L. Shur, "A new version of detached eddy simulation, resistant to ambiguous grid densities," *Theoretical and computational fluid dynamics*, vol. 20, pp. 181-195, Dec. 2006.
[15] S. R. Wellborn, B. A. Reichert, T. H. Okiishi, "An experimental investigation of the flow in a diffusing S-duct," in *Proc. 28th Joint Propulsion Conference and Exhibit*, Nashville, 1992, pp. 1–13.
[16] S. Berhm, T. Kachele, R. Niehuis, "CFD Investigations on the Influence of varying Inflow Conditions on the Aerodynamics in an S-Shaped Inlet Duct," *AIAA Journal*, vol. 51, pp. 462-474, Jul. 2014.
[17] M. K. Gopaliya, P. Jain, S. Kumar, "Performance improvement of s-shaped diffuser using momentum imparting technique," *IOSR Journal*

of Mechanical and Civil Engineering, vol. 11, pp. 23-31, Mar. 2014.
[18] S. ge, R. Cui, "Design and numerical simulation of submerged s-shaped inlet duct," *Electrical Engineering & Automation*, vol. 2, no. 4, pp. 44-51, Apr. 2013.